Large-Deformation Instability Behaviors of 3D Beams Supported with 3D Hinge Joints Subjected to Axial and Torsional Loadings

A.R. Damanpack[1†] and M. Bodaghi[2]

[1]*Department of Technology and Innovation, University of Southern Denmark, Odense, Denmark*

[2]*Department of Engineering, School of Science and Technology, Nottingham Trent University, Nottingham NG11 8NS, United Kingdom*

Abstract

In this paper, an instability analysis of three-dimensional (3D) beams supported with 3D hinges under axial and torsional loadings is presented in large displacement and rotation regime. An exact displacement field is proposed based on the central line and orientation of the cross-section consisting of nine parameters corresponded to 3D centroid movements and rotations. Cauchy-Green deformation tensor is derived in the local coordinate system according to the proposed displacement field. Deformation tensor and a normal-shear constitutive model with highly polynomial non-linearity are developed based on the continuum mechanics. A finite element formulation is then established based on the higher order shape functions to avoid shear and membrane locking issues. The elemental governing equations of equilibrium as well as 3D nodal forces and moments are obtained using the Hamiltonian principle. To solve the final nonlinear equilibrium equations, Newton-Raphson and Riks techniques through an incremental-iterative scheme are implemented. The numerical results are presented to assess instability behaviors of beams with different cross sections and various 3D boundary conditions. The effects of 3D hinge joints on the stability of beams under axial and torsional loadings are studied for the first time. The numerical results reveal instability in bending and lateral-torsional buckling for beams supported by 3D hinge joints. This phenomenon is proved by both finite strain model and its linearization for small deformations. The numerical results show that the present finite element formulation is robust, reliable as well as simple and easy to model instability of 3D beams in the large displacement regime.

Keywords: *Instability, Post-buckling, 3D beams, 3D hinge joints, Finite strain, Finite element method*

[†] Corresponding Author,
Tel.: +45 6550 9470; *E-mail addresses:* adpm@sdu.dk , ardamanpack@gmail.com

1. Introduction

Accurate and simple beam or plate theories are always demanded by engineers and scientists. In contrast to plates and shells, thin rods or beam-like structures usually experience large displacements and typically rotations without exceeding the material elastic limit. This substantial changes in the equilibrium configurations demand a proper and adapted mathematical model. There have been various types of strategies and methods to implement large rotations through the deformation fields, see e.g. Refs. [1-27]. Reissner [1] proposed a large deformation theory of space-curved lines with applied forces and moments on each cross section. A system of equilibrium equations was obtained by the virtual work based on the one-dimensional (1D) constitutive equation for in-plane 3D beam problems. Reissner [1,2] and Simo [3] could be considered as pioneers who developed geometrically exact beam models and their approaches were widely used by other researchers [1-6]. However, based on the Kirchhoff constraints [7], the shear strains may be ignored when beams are slender enough. In this case, the rotation of cross-section can be expressed by a tangent vector of the beam axis. This assumption can reduce the number of equilibrium equations as well as prevent shear locking issues. Based on Simo-Ressner 3D beam theory, some researches were performed on formulation, solution method, eliminating shear and membrane locking phenomenon and satisfying Kirchhoff constraints. Ibrahimbegovic [8] developed a non-locking finite element interpolation for 3D Reissner beam which can remove both shear and normal locking. Meier *et al.* [9, 10] developed a finite element approach based on 3D Reissner theory for slender beams with arbitrary cross section and curve geometries. They used an orthogonal interpolation to satisfy Kirchhoff constraints and remove shear components of the strain tensor. They also employed Hermite shape functions to describe the deformation functions along the beam axis. Following this approach, they extended their finite element formulation for 3D beams to overcome membrane locking phenomenon. For this purpose, they used another interpolation approach for normal strains when beams are very slender. Hodges [11] developed a weak form of the partial differential equations of motion for a deep, symmetric beam under the action of a tip follower force acting in the plane of symmetry. He obtained an approximate solution using cantilever beam bending and torsional modes. Yu et al. [12] illustrated the procedure of constructing a generalized variational asymptotic beam sectional analysis for composite beams and variational-asymptotic method and provided some benchmark results with which other theories could be compared.

The co-rotational formulation is another approach which decomposes the displacement field into rigid body motions and deformations. In this concept, local reference configuration is employed to define the deformed configuration. It means that the reference frame moves and rotates but never deforms. When elements are small enough, the linear or modified nonlinear strains can be used in the reference configuration. This approach of 3D beam element so-called co-rotational formulation is widely used [13-16]. Some researchers used Lagrangian formulation to extract governing equations for 3D beam structures. Bathe and Bolourchi [4] employed two different formulation of total Lagrangian and updated Lagrangian for extracting stiffness matrices

of 3D beam elements in large displacement and rotation regime. Gimena *et al.* [17] obtained a linear ordinary system of equations for analysis of 3D beams with different curved geometries such as elliptical or helical arcs. They mainly focused on developing both analytical and numerical approaches to solve these equations. Damanpack *et al.* [18] developed a 3D finite strain model for analysis of 2D beam problems in the large deformation regime. The model was proposed based on Green-Lagrangian strain tensor and hyper-elastic Mooney-Rivlin strain energy function. They implemented the model to simulate experimental snap-through and large deformation of curved beams. Some researches have been dedicated to analyzing 3D beams and frames by considering out-of-plane deformations and warping effects under torsions. Atluri *et al.* [19] developed a finite element formulation for 3D beam theory. They considered shear deformations and warping effects of cross sections. Coda [20] used a solid-like approach for finite element formulating of 3D inhomogeneous beams and frames. The warping mode was calculated based on Saint-Venant theory in different parts of the solving process. Manta and Goncalves [21] developed a finite element formulation for 3D beam by considering Kirchhoff constraints and torsion warping. They also studied the effect of cross-section geometries in the large deformation regime. Vo and·Nanakorn [22] presented a new total Lagrangian Timoshenko beam formulation with the isogeometric analysis approach for a geometrically nonlinear analysis of planar curved beams.

Beam-like structures under full or partial compressive/bending loading are prone to failure by the buckling phenomenon [23]. This phenomenon has been studied by many researchers through case studies and numerical techniques. Cardona and Huespe [24] focused on developing an efficient and reliable algorithm to compute lateral buckling and distinguish bifurcation point of 3D beams, arches and frames. They also considered a wide range of aspect ratios for 3D beams with rectangular cross-sections. Levyakov [25] developed a finite element formulation for the analysis of 3D beams or rods by considering shear deformations. He also studied some examples in the large deformation and post-buckling regime. Liao *et al.* [22] also presented a differential quadrature formulation for post-buckling analysis of beams and 2D frames. Small displacements and rotations for an elastic domain were considered to derive equilibrium equations and stiffness matrix. Cottanceau *et al.* [27] presented a quasi-static formulation for flexible 3D beams based on the geometrically exact theory and rotational quaternions. A finite element method was employed to discretize equilibrium equations. The buckling and post-buckling of beams and frames were considered and compared with experiments. Gonçalves [28] used the geometrically exact 3D beam theory to simulate I-section structures undergoing bending and lateral-torsional buckling. They studied I-sections with standard height-to-width ratios and cantilever and simply supported boundary conditions (BCs). They numerically investigated different post-buckling behaviors of beam structures by standard cross sections. Recently, Weeger *et al.* [29] used an isogeometric method for analysis of 3D beams and rods based on the geometrically exact Cosserat rod theory. They also employed the gradient-based algorithms to solve the equilibrium equations under large deformation and rotation regime. For evaluation of sensibility of calculations, they introduced different methods such as semi-analytical, inconsistent analytical and fully analytical approaches. Through a case study, post-buckling of curved beams also was studied.

As reviewed above, buckling and post-buckling of 3D beams and frames have been studied by considering different situations except 3D boundary conditions. In this paper, for the first time, the effects of 3D hinge supports on the large-deformation instability of 3D beams under axial and torsional loadings are investigated. A geometrically exact 3D displacement field is assumed by a movement vector and an orthogonal rotation tensor. The Hamiltonian principle is employed to extract equilibrium equations by considering Cauchy-Green deformation tensor and Hooke constitutive equation. The governing equations are solved by establishing a finite element formulation based on the higher order shape functions to eliminate shear and membrane locking phenomena. Newton-Raphson method and Riks technique are implemented to solve the nonlinear system of equations. The accuracy and efficiency of the presented formulation is verified through some numerical studies. After validation, buckling, post-buckling behaviors of 3D hinge supported beams under axial and torsional loading are studied in detail. Due to the absence of similar model in the specialized literature, the proposed model and solution can be instrumental in the analysis and design of 3D beams with 3D hinge supports under axial and torsional loadings.

2. 3D beam theory

2.1. Geometrically exact formulation

Fig. 1 shows a 3D beam element in the global coordinate system located on the mid-plane of beam. It is assumed that beam element is straight at the initial or reference configuration (x_1, x_2, x_3) as illustrated in Fig. 1a. The curved element can be mapped by means of standard iso-parametric mapping or considered as a stress-free deformed configuration from the straight reference configuration. By ignoring the effect of rotations and cross-section warping [16, 25, 27], the deformed configuration $(\overline{x}_1, \overline{x}_2, \overline{x}_3)$ can be expressed by the 3D centroid movement and orthogonal rotation in the reference configuration as follows:

$$\overline{x} = x_o + u + q(x - x_o) \tag{1}$$

where x_o and u are centroid position and movement, respectively, while q denotes the orthogonal rotation tensor. It is geometrically exact since displacements and rotations are large, and the finite strain is involved. The orthogonal rotation tensor also is constrained by the following equation:

$$qq^T = q^Tq = I \tag{2}$$

where I is the second order identity tensor. Regarding Eq. (2), the orthogonal rotation tensor as well as its consistency conditions are considered as:

$$q = \begin{bmatrix} q_{22}q_{33} - q_{23}q_{32} & q_{12} & q_{13} \\ q_{13}q_{32} - q_{12}q_{33} & q_{22} & q_{23} \\ q_{12}q_{23} - q_{13}q_{22} & q_{32} & q_{33} \end{bmatrix} \tag{3}$$

$$q_{12}^2 + q_{22}^2 + q_{32}^2 = 1$$
$$q_{13}^2 + q_{23}^2 + q_{33}^2 = 1 \tag{4}$$
$$q_{12}q_{13} + q_{22}q_{23} + q_{32}q_{33} = 0$$

The relationship between components of rotation matrix and rotations of axes in the reference configuration as demonstrated in Fig. 1b can be defined as:

$$\theta_{21} = -\tan^{-1}(q_{31}/q_{11}); \quad \theta_{31} = \tan^{-1}(q_{21}/q_{11})$$

$$\theta_{12} = \tan^{-1}(q_{32}/q_{22}); \quad \theta_{32} = -\tan^{-1}(q_{12}/q_{22}) \tag{5}$$

$$\theta_{13} = -\tan^{-1}(q_{23}/q_{33}); \quad \theta_{23} = \tan^{-1}(q_{13}/q_{33})$$

in which θ_{ij} ($i = 1,2,3$) represents the rotation angle of x_j-axis around x_i-axis. According to the proposed displacement field (1), the deformation gradient tensor $\boldsymbol{F}$ and the right Cauchy-Green deformation tensor $\boldsymbol{C}$ can be determined as:

$$\boldsymbol{F} = \overline{\boldsymbol{x}}_{,x} \qquad F_{ij} = \frac{\partial \overline{x}_i}{\partial x_j} \quad i,j = 1,2,3 \tag{6}$$

$$\boldsymbol{C} = \boldsymbol{F}^T \boldsymbol{F} \tag{7}$$

By considering the orthogonality of rotation tensor $\boldsymbol{q}$ and substituting Eq. (1) into Eqs. (6) and (7), the right Cauchy-Green deformation tensor is derived as:

$$\boldsymbol{C} = \begin{bmatrix} C_{11} & C_{12} & C_{13} \\ C_{12} & 1 & 0 \\ C_{13} & 0 & 1 \end{bmatrix} \tag{8}$$

$$\boldsymbol{E} = \tfrac{1}{2}(\boldsymbol{C} - \boldsymbol{I}) \tag{9}$$

where $\boldsymbol{E}$ represents the Green-Lagrange strain tensor. According to Eq. (8), the 3D beams experience a normal axial deformation and two transverse shear deformations during mechanical loading. By ignoring the high-order terms of x_2 and x_3, the components of $\boldsymbol{E}$ can be obtained as:

$$E_{11} = \tfrac{1}{2}(C_{11} - 1) = u_{1,1} + \tfrac{1}{2}(u_{1,1}^2 + u_{2,1}^2 + u_{3,1}^2)$$
$$+ x_2\big(q_{12,1}(1 + u_{1,1}) + q_{22,1}u_{2,1} + q_{32,1}u_{3,1}\big)$$
$$+ x_3\big(q_{13,1}(1 + u_{1,1}) + q_{23,1}u_{2,1} + q_{33,1}u_{3,1}\big);$$
$$2E_{12} = C_{12} = q_{12} + (q_{12}u_{1,1} + q_{22}u_{2,1} + q_{32}u_{3,1}) + x_2(q_{12}q_{12,1} + q_{22}q_{22,1}$$
$$+ q_{32}q_{32,1}) + x_3(q_{12}q_{13,1} + q_{22}q_{23,1} + q_{32}q_{33,1})$$
$$2E_{13} = C_{13} = q_{13} + (q_{13}u_{1,1} + q_{23}u_{2,1} + q_{33}u_{3,1}) + x_2(q_{13}q_{12,1} + q_{23}q_{22,1}$$
$$+ q_{33}q_{32,1}) + x_3(q_{13}q_{13,1} + q_{23}q_{23,1} + q_{33}q_{33,1}) \tag{10}$$
$$2E_{22} = q_{12}^2 + q_{22}^2 + q_{32}^2 - 1$$
$$2E_{33} = q_{13}^2 + q_{23}^2 + q_{33}^2 - 1$$
$$2E_{23} = q_{12}q_{13} + q_{22}q_{23} + q_{32}q_{33}$$

Considering orthogonality conditions in Eq. (4) (e.g., $q_{12}^2 + q_{22}^2 + q_{32}^2 = 1$), it can be found that $E_{22} = E_{33} = E_{23} = 0$. This is consistent with the strain field derived in Ref. [4, 5, 15, 16, 19, 21, 22, 27, 28].

2.2. 2D beam theory

The proposed geometrically exact 3D equation is a general form that can be simplified for a planar case. To this end, all movements and rotations are constrained on the $x_1 - x_3$ plane and the following assumptions (11) and (12) are applied on Eq. (1). The result of deformed configurations is called 2D theory of beam or a special case of geometrically exact formulation.

$$u_2 = 0$$
$$\theta_{31} = \theta_{13} = \theta_{12} = \theta_{32} = 0 \tag{11}$$
$$\theta_{21} = \theta_{23} = \theta_2$$

in which θ_2 is the pure rotation angle along x_2-axis [30].

$$E_{11} = \tfrac{1}{2}(C_{11} - 1) = u_{1,1} + \tfrac{1}{2}(u_{1,1}^2 + u_{3,1}^2) + x_3\theta_{2,1}((1 + u_{1,1})\cos\theta_2 - u_{3,1}\sin\theta_2)$$
$$2E_{13} = C_{13} = (1 + u_{1,1})\sin\theta_2 + u_{3,1}\cos\theta_2 \tag{12}$$

2.3. 3D beam theory with small rotations and displacements

For small rotations and displacements, the 3D geometrical equations can be linearized by neglecting nonlinear parameters in the displacement field as follows:

$$q = \begin{bmatrix} 1 & -\theta_3 & \theta_2 \\ \theta_3 & 1 & -\theta_1 \\ -\theta_2 & \theta_1 & 1 \end{bmatrix} \tag{13}$$

where θ_1, θ_2 and θ_3 are the pure small rotation angles along x_1, x_2 and x_3-axes, respectively.

$$E_{11} = \tfrac{1}{2}(C_{11} - 1) = u_{1,1} - x_2\theta_{3,1} + x_3\theta_{2,1}$$
$$2E_{12} = C_{12} = u_{2,1} - \theta_3 - x_3\theta_{1,1} \tag{14}$$
$$2E_{13} = C_{13} = u_{3,1} + \theta_2 + x_2\theta_{1,1}$$

3. Material constitutive model

In this section, the selected constitutive equation is adapted to a 3D beam theory which consists of normal-shear strain field. For isotropic materials, the strain energy density function W can be expressed in terms of the invariants of right Cauchy-Green deformation tensor:

$$W = \overline{W}(I_1, I_2, J) = \widetilde{W}(\overline{I}_1, \overline{I}_2, J) \tag{15}$$

where:

$$I_1 = trace\,(\boldsymbol{C}) \quad I_2 = \tfrac{1}{2}(trace(\boldsymbol{C})^2 - trace(\boldsymbol{C}^2)) \quad J^2 = det(\boldsymbol{C}) \tag{16}$$
$$\overline{I}_1 = J^{\frac{-2}{3}}I_1 \qquad \overline{I}_2 = J^{\frac{-4}{3}}I_2 \tag{17}$$

6

By considering Eq. (15), the second Piola–Kirchhoff stress tensor $\boldsymbol{S}$ can be derived for hyper-elastic materials as:

$$\boldsymbol{S} = 2\frac{\partial W}{\partial \boldsymbol{C}} \tag{18}$$

and

$$
\begin{aligned}
\boldsymbol{S} &= 2\left(\frac{\partial \overline{W}}{\partial I_1} + I_1\frac{\partial \overline{W}}{\partial I_2}\right)\boldsymbol{I} - 2\frac{\partial \overline{W}}{\partial I_2}\boldsymbol{C} + J\frac{\partial \overline{W}}{\partial J}\boldsymbol{C}^{-1}\\
&= 2J^{-\frac{2}{3}}\left(\frac{\partial \widetilde{W}}{\partial \bar{I}_1} + \bar{I}_1\frac{\partial \widetilde{W}}{\partial \bar{I}_2}\right)\boldsymbol{I} - 2J^{-\frac{4}{3}}\frac{\partial \widetilde{W}}{\partial \bar{I}_2}\boldsymbol{C} + J\left(\frac{\partial \widetilde{W}}{\partial J} - \frac{2}{3J}\left(\bar{I}_1\frac{\partial \widetilde{W}}{\partial \bar{I}_1} + 2\bar{I}_2\frac{\partial \widetilde{W}}{\partial \bar{I}_2}\right)\right)\boldsymbol{C}^{-1}
\end{aligned}
\tag{19}
$$

The simplest strain energy is the Saint Venant–Kirchhoff model which just covers the linear elastic material in the finite strain regime. This strain energy can be written as:

$$W = \overline{W}(I_1, I_2) = \frac{\lambda}{8}(I_1 - 3)^2 + \frac{\mu}{4}(I_1^2 - 2I_1 - 2I_2 + 3) \tag{20}$$

where λ and μ are the Lame parameters. For this case, the constitutive equation adapted with the proposed 3D beam theory can be expressed by following right Cauchy–Green deformation tensor:

$$\boldsymbol{C} = \begin{bmatrix} C_{11} & C_{12} & C_{13} \\ C_{12} & C_{22} & 0 \\ C_{13} & 0 & C_{33} \end{bmatrix} \qquad C_{22} = C_{33} = (1 + v) - vC_{11}; \qquad v = \frac{1}{2}\lambda/(\lambda + \mu) \tag{21}$$

where v is known as Poisson's ratio. The second Piola–Kirchhoff stress tensor can be extracted by substituting Eq. (20) into Eq. (19) and assuming the plane stress hypothesis as:

$$
\begin{aligned}
&S_{22} = S_{33} = S_{23} = 0\\
&S_{11} = \frac{1}{2}E(C_{11} - 1) \qquad S_{12} = \mu C_{12} \qquad S_{13} = \mu C_{13}; \qquad E = \mu(3\lambda + 2\mu)/(\lambda + \mu)
\end{aligned}
\tag{22}
$$

in which E represents Young modulus of the material. Eq. (22) is consistent with the stress field derived in Ref. [4, 5, 15, 16, 19, 21, 22, 27, 28] for finite strains.

4. Finite element modeling

4.1. Governing partial equations

Beam- and rod-like structures are widely used for many engineering fields. In many engineering applications, beams undergo a combined axial-shear deformation which can be modeled by 3D beam elements. Therefore, in this section, a finite element formulation is developed to analyze 3D elastic beams and frames in the finite strain regime.

In order to extract governing equations of equilibrium for the proposed 3D beam element, the Hamiltonian principle is implemented as:

$$\delta W_{in} = \delta W_{ext} \tag{23}$$

where δ and W_{in} represent first variation and total internal energy, respectively. W_{ext} also is the external work applied by mechanical loads. For the proposed 3D beam element, the variational of total internal energy can be expressed as:

$$\delta W_{in} = \frac{1}{2} \int_{\tilde{V}} (\delta C_{11} S_{11} + 2\delta C_{12} S_{12} + 2\delta C_{13} S_{13}) d\tilde{V} \tag{24}$$

where $\tilde{V}$ is the volume. According to the beam theories, external loads usually consist of centroid forces and moments. For the proposed model, the external forces are applied directly on the central point of each cross section. As demonstrated in Fig. 1a, the external moments can be enforced by applying two force vectors on A and B along x_2 and x_3-axes, respectively. It is stated as:

$$\boldsymbol{x}_{oA} = \boldsymbol{x}_A - \boldsymbol{x}_o = [0 \ 1 \ 0]^T \quad \Rightarrow \quad \overline{\boldsymbol{x}}_{oA} = [q_{12} \ q_{22} \ q_{32}]^T \tag{25}$$

$$\boldsymbol{x}_{oB} = \boldsymbol{x}_B - \boldsymbol{x}_o = [0 \ 0 \ 1]^T \quad \Rightarrow \quad \overline{\boldsymbol{x}}_{oB} = [q_{13} \ q_{23} \ q_{33}]^T \tag{26}$$

According to the external load field, the virtual work of external load applying on each cross section is determined by:

$$\delta W_{ext} = [\delta u_1 \ \delta u_2 \ \delta u_3] \boldsymbol{f}_o + [\delta q_{12} \ \delta q_{22} \ \delta q_{32}] \boldsymbol{f}_A + [\delta q_{13} \ \delta q_{23} \ \delta q_{33}] \boldsymbol{f}_B \tag{27}$$

where $\boldsymbol{f}_o$, $\boldsymbol{f}_A$ and $\boldsymbol{f}_B$ are the external force vectors along the local coordinate axes and applied on o, A and B, respectively. By substituting Eqs. (12), (24) and (27) into Eq. (23) and simplifying the Hamiltonian principle using the fundamental lemma of calculus of variations, we can obtain the integral form of governing partial equations as:

$$\int_0^l [\delta u_1 \ \delta u_2 \ \delta u_3] \left(\int_{\tilde{A}} \frac{1}{2} \left(\left\{ \begin{matrix} \frac{\partial C_{11}}{\partial u_o} \\ \frac{\partial C_{11}}{\partial v_o} \\ \frac{\partial C_{11}}{\partial w_o} \end{matrix} \right\} S_{11} + \left\{ \begin{matrix} \frac{\partial C_{12}}{\partial u_o} \\ \frac{\partial C_{12}}{\partial v_o} \\ \frac{\partial C_{12}}{\partial w_o} \end{matrix} \right\} S_{12} + \left\{ \begin{matrix} \frac{\partial C_{13}}{\partial u_o} \\ \frac{\partial C_{13}}{\partial v_o} \\ \frac{\partial C_{13}}{\partial w_o} \end{matrix} \right\} S_{13} \right) d\tilde{A} - \boldsymbol{f}_o \right) dx = \boldsymbol{0} \tag{28}$$

$$\int_0^l [\delta q_{12} \ \delta q_{22} \ \delta q_{32}] \left(\int_{\tilde{A}} \frac{1}{2} \left(\left\{ \begin{matrix} \frac{\partial C_{11}}{\partial q_{12}} \\ \frac{\partial C_{11}}{\partial q_{22}} \\ \frac{\partial C_{11}}{\partial q_{32}} \end{matrix} \right\} S_{11} + \left\{ \begin{matrix} \frac{\partial C_{12}}{\partial q_{12}} \\ \frac{\partial C_{12}}{\partial q_{22}} \\ \frac{\partial C_{12}}{\partial q_{32}} \end{matrix} \right\} S_{12} + \left\{ \begin{matrix} \frac{\partial C_{13}}{\partial q_{12}} \\ \frac{\partial C_{13}}{\partial q_{22}} \\ \frac{\partial C_{13}}{\partial q_{32}} \end{matrix} \right\} S_{13} \right) d\tilde{A} - \boldsymbol{f}_A \right) dx = \boldsymbol{0} \tag{29}$$

$$\int_0^l [\delta q_{13} \ \delta q_{23} \ \delta q_{33}] \left(\int_{\tilde{A}} \frac{1}{2} \left(\left\{ \begin{matrix} \frac{\partial C_{11}}{\partial q_{13}} \\ \frac{\partial C_{11}}{\partial q_{23}} \\ \frac{\partial C_{11}}{\partial q_{33}} \end{matrix} \right\} S_{11} + \left\{ \begin{matrix} \frac{\partial C_{12}}{\partial q_{13}} \\ \frac{\partial C_{12}}{\partial q_{23}} \\ \frac{\partial C_{12}}{\partial q_{33}} \end{matrix} \right\} S_{12} + \left\{ \begin{matrix} \frac{\partial C_{13}}{\partial q_{13}} \\ \frac{\partial C_{13}}{\partial q_{23}} \\ \frac{\partial C_{13}}{\partial q_{33}} \end{matrix} \right\} S_{13} \right) d\tilde{A} - \boldsymbol{f}_B \right) dx = \boldsymbol{0} \tag{30}$$

where l and $\tilde{A}$ are the length and the cross section of the beam element, respectively.

4.2. Finite element formulation

To avoid shear and membrane locking issues, the quadratic shape functions are employed for interpolating of the displacement variables in the local coordinate as:

$$
\begin{aligned}
u_1 &= N_1 u_e & N_1 &= [N_1\ 0\cdots 0\ N_2\ 0\cdots 0\ N_3\ 0\ 0\ 0\ 0\ 0\ 0\ 0]_{1\times 27} \\
u_2 &= N_2 u_e & N_2 &= [0\ N_1\ 0\cdots 0\ N_2\ 0\cdots 0\ N_3\ 0\ 0\ 0\ 0\ 0\ 0]_{1\times 27} \\
u_3 &= N_3 u_e & N_3 &= [0\ 0\ N_1\ 0\cdots 0\ N_2\ 0\cdots 0\ N_3\ 0\ 0\ 0\ 0\ 0]_{1\times 27} \\
q_{12} &= N_4 u_e & N_4 &= [0\ 0\ 0\ N_1\ 0\cdots 0\ N_2\ 0\cdots 0\ N_3\ 0\ 0\ 0\ 0]_{1\times 27} \\
q_{22} &= N_5 u_e & N_5 &= [0\ 0\ 0\ 0\ N_1\ 0\cdots 0\ N_2\ 0\cdots 0\ N_3\ 0\ 0\ 0]_{1\times 27} \\
q_{23} &= N_6 u_e & N_6 &= [0\ 0\ 0\ 0\ 0\ N_1\ 0\cdots 0\ N_2\ 0\cdots 0\ N_3\ 0\ 0\ 0]_{1\times 27} \\
q_{13} &= N_7 u_e & N_7 &= [0\ 0\ 0\ 0\ 0\ 0\ N_1\ 0\cdots 0\ N_2\ 0\cdots 0\ N_3\ 0\ 0]_{1\times 27} \\
q_{23} &= N_8 u_e & N_8 &= [0\ 0\ 0\ 0\ 0\ 0\ 0\ N_1\ 0\cdots 0\ N_2\ 0\cdots 0\ N_3\ 0]_{1\times 27} \\
q_{33} &= N_9 u_e & N_9 &= [0\ 0\ 0\ 0\ 0\ 0\ 0\ 0\ N_1\ 0\cdots 0\ N_2\ 0\cdots 0\ N_3]_{1\times 27}
\end{aligned}
\tag{31}
$$

where u_e indicates elemental displacement vector in the local coordinate and $N_i (i = 1,2,3)$ are quadratic Lagrange shape functions [30] defined as:

$$
N_1 = \frac{x_1}{l}\left(1 - 2\frac{x_1}{l}\right) \qquad N_2 = \left(1 + 2\frac{x_1}{l}\right)\left(1 - 2\frac{x_1}{l}\right) \qquad N_3 = \frac{x_1}{l}\left(1 + 2\frac{x_1}{l}\right)
\tag{32}
$$

$$
\begin{aligned}
u_e &= [u_1\ u_2\ u_3]^T \\
u_i &= [\,u_1\ u_2\ u_3\ q_{12}\ q_{22}\ q_{23}\ q_{13}\ q_{23}\ q_{33}]_i^T \quad ; \quad i = 1,2,3
\end{aligned}
\tag{33}
$$

where u_i represents nodal displacement of the ith node. By substituting the discretized displacement variables (31) into (10), the right Cauchy-Green deformation tensor can be expressed in terms of u_e as:

$$
\begin{aligned}
C_{11} &= 1 + N_{C_{11}}(x, u_e)u_e \\
C_{12} &= N_{C_{12}}(x, u_e)u_e \\
C_{13} &= N_{C_{13}}(x, u_e)u_e
\end{aligned}
\tag{34}
$$

where their first variation is given by:

$$
\begin{aligned}
\delta C_{11} &= N_{C_{11}}\delta u_e \\
\delta C_{12} &= N_{C_{12}}\delta u_e \\
\delta C_{13} &= N_{C_{13}}\delta u_e
\end{aligned}
\tag{35}
$$

The governing equations of equilibrium for the elastic 3D beam element can be determined in the matrix form by substituting Eqs. (31) and (35) plus constitutive equations (22) into (28)-(30) and calculating the elemental integrals as:

$$
\underline{g}_e(u_e) = \underline{f}_e
\tag{36}
$$

where $\underline{f}_e$ and $\underline{g}_e$ are the elemental force vectors corresponded to external and internal energies, respectively, defined as:

$$\underline{g}_e = \begin{bmatrix} \underline{g}_1^T & \underline{g}_2^T & \underline{g}_3^T \end{bmatrix}^T; \qquad \underline{g}_i = \begin{bmatrix} \underline{g}_o^T & \underline{g}_A^T & \underline{g}_B^T \end{bmatrix}_i^T \quad ; i = 1,2,3 \tag{37}$$

$$\underline{f}_e = \begin{bmatrix} \underline{f}_1^T & \underline{f}_2^T & \underline{f}_3^T \end{bmatrix}^T; \qquad \underline{f}_i = \begin{bmatrix} \underline{f}_o^T & \underline{f}_A^T & \underline{f}_B^T \end{bmatrix}_i^T \quad ; i = 1,2,3 \tag{38}$$

$\underline{g}_i$ and $\underline{f}_i$ are the nodal external forces applied on the ith node.

4.3. Developing centroid forces and moments

By using Eqs. (25) and (26), the centroid external moment can be given in terms of external forces enforced on A and B as follows:

$$\begin{aligned} \boldsymbol{m}_o &= \overline{\boldsymbol{x}}_{oA} \times \boldsymbol{f}_A + \overline{\boldsymbol{x}}_{oB} \times \boldsymbol{f}_B \\ &= [q_{12}\, q_{22}\, q_{32}]^T \times \boldsymbol{f}_A + [q_{13}\, q_{23}\, q_{33}]^T \times \boldsymbol{f}_B \end{aligned} \tag{39}$$

Therefore, the governing equations (36) can be modified based on the 3D beam element presented in Fig. 2a in terms of centroid external forces and moments as follows:

$$\boldsymbol{g}_e(\boldsymbol{u}_e) = \boldsymbol{f}_e \tag{40}$$

in which

$$\boldsymbol{g}_e = \begin{bmatrix} \boldsymbol{g}_1^T & \boldsymbol{g}_2^T & \boldsymbol{g}_3^T \end{bmatrix}^T \tag{41}$$

$$\boldsymbol{g}_i = \begin{bmatrix} \underline{g}_o^T & \left(\overline{\boldsymbol{x}}_{oA} \times \underline{g}_A + \overline{\boldsymbol{x}}_{oB} \times \underline{g}_B \right)^T & \overline{\boldsymbol{x}}_{oA}^T \overline{\boldsymbol{x}}_{oA} & \overline{\boldsymbol{x}}_{oB}^T \overline{\boldsymbol{x}}_{oB} & \overline{\boldsymbol{x}}_{oA}^T \overline{\boldsymbol{x}}_{oB} \end{bmatrix}_i^T \quad ; i = 1,2,3$$

where $\overline{\boldsymbol{x}}_{oA}^T \overline{\boldsymbol{x}}_{oA}$, $\overline{\boldsymbol{x}}_{oB}^T \overline{\boldsymbol{x}}_{oB}$ and $\overline{\boldsymbol{x}}_{oA}^T \overline{\boldsymbol{x}}_{oB}$ are three orthogonality consistency conditions which must be enforced directly on the rotational nodal variables. On the other hand, $\boldsymbol{f}_e$ represents the modified elemental external forces and moments expressed by:

$$\boldsymbol{f}_e = \begin{bmatrix} \boldsymbol{f}_1^T & \boldsymbol{f}_2^T & \boldsymbol{f}_3^T \end{bmatrix}^T; \qquad \boldsymbol{f}_i = [\boldsymbol{f}_o^T \; \boldsymbol{m}_o^T \; 1 \; 1 \; 0]_i^T \; ; i = 1,2,3 \tag{42}$$

in which $\boldsymbol{f}_o$ and $\boldsymbol{m}_o$, as mentioned above, are the external centroid force and moment vectors, respectively.

Following this formulation, boundary conditions can be applied by constraining nodal displacements and rotations. The 3D hinge support is represented by H which can be considered for demonstration of both displacement and rotational conditions, see Fig. 2b. As shown in Fig. 2b, a general 3D direction of $\overrightarrow{\alpha\beta}$ is considered for applying nodal constraints. This direction is defined by two angles of α and β based on the spherical coordinate. According to 3D hinge conditions, various types of displacement and rotational constraints can be applied on the corresponded nodes as described in Table 1.

4. Numerical results

4.1. Validation

In this section, the buckling and post-buckling behaviors of 3D beams under mechanical loadings are investigated. The presented model is implemented in MATLAB software package through Newton-Raphson framework. In the solution process, Riks technique [31] is employed to trace non-linear deformation and/or loading paths. The beams subjected to in-plane force or torsional moment are studied in the large displacement regime. In following results, f_c represents the buckling force of simply supported Euler beam and is considered as a benchmark force to assess in-plane forces. It is defined as:

$$f_c = \frac{\pi^2 EI}{L^2} \tag{43}$$

where I is minimum area moment of inertia of the cross section of the beam.

For validating the present model in terms of accuracy and capabilities, the response of a fully clamped beam under in-plane load as one of the most difficult problems is studied as presented in Fig. 3. In this case, a slender beam with circular cross section $(L = 1\ m$ and $R = 0.02m)$ made of linear elastic materials $(E = 105\ GPa$ and $\nu = 0.3)$ is considered. This problem has been investigated by some researchers [25, 27] using different numerical methods. In Fig. 3, the post-buckling path of a fully clamped slender beam is presented and compared with numerical results from Ref. [27]. As can be seen, the first buckling occurs at $4f_c$ corresponded to the critical force of fully clamped Euler beams. By tracing the post-buckling path, it is found that configuration is unstable, and the bifurcation happens at $5.56f_c$ in the 3D beam model. In terms of accuracy, the bifurcation point is obtained $5.56f_c$ against $5.61f_c$ reported in Ref. [27]. The comparison of post-buckling paths as presented in Fig.3 shows that there is a good agreement between present results and those from Ref. [27] that verifies the accuracy of the present model and solution technique for complex and nonlinear cases.

The geometrical and material properties for the following simulation are set as: length $=$ $20\pi\ mm$, circular cross section of radius $R = 1\ mm$, rectangular cross section of width/height $\frac{b}{h} = 2, b = \sqrt{2\pi}\ mm$, Young's modulus $E = 23.4\ MPa$ and Poisson's ratio $\nu = 0.3$. The 3D boundary conditions in this study are listed in Table 2.

4.2. Straight beams under in-plane loads

For finding the first snap point along the buckling path, a simplified linear form of the present model (13) is employed to determine buckling loads as well as corresponding mode shapes. For the small deformation/rotation fields (14) and linear elastic materials (22), the equilibrium equations of the beam element can be obtained from the Hamiltonian principle (23) as follows:

$$\int_0^l \left(E\left(I_{22}\,\delta\theta_{3,1}\theta_{3,1} + I_{33}\,\delta\theta_{2,1}\theta_{2,1}\right) + \mu(I_{22} + I_{33})\,\delta\theta_{1,1}\theta_{1,1} + \right.$$
$$\left. \mu A\left(\left(\delta u_{3,1} - \delta\theta_2\right)\left(u_{3,1} - \theta_2\right) + \left(\delta u_{2,1} + \delta\theta_3\right)\left(u_{2,1} + \theta_3\right)\right) - f_*\left(\delta u_{2,1}u_{2,1} + \delta u_{3,1}u_{3,1}\right)\right) dx = 0 \tag{44}$$

where f_* is the axial load. I_{22}, I_{33} and A also represent moments of inertia and area of the beam cross section, respectively. After implementing the finite element method and applying boundary conditions, an eigenvalue problem is obtained. The eigenvalues and eigenvectors represent the buckling loads and corresponding shape modes, respectively.

Fig. 4 shows the variation of critical in-plane buckling force of beams with various boundary conditions. Based on Table 2, the rotations of the beam for BC1 are constrained around $\overrightarrow{0\beta}$-axis by means of a 3D hinge at the first edge and clamped at the end. As explained in Fig. 2 and Table 1, $\overrightarrow{0\beta}$-axis is perpendicular to the x_3-axis, so that $\overrightarrow{0\beta}$-axis refers to x_1 and x_2-axes by $\beta = 0$ and $\frac{\pi}{2}$, respectively. In the small deformation/rotation regime under a bending condition, this 3D hinge acts like clamped and simply-supported boundary conditions for $\beta = 0$ and $\frac{\pi}{2}$, respectively. In this case, increasing β-angle decreases the buckling force because of reduction in the stiffness at hinge support and changes the buckling mode shape, see Fig. 4a. According to the Euler beam theory, the buckling shape mode transforms from the 1st mode of clamped-clamped ($4f_c$) to the 1st mode of simply-supported-clamped conditions ($2.04f_c$). The following results presented in Fig. 5-9 will show that the buckling shape modes or beam configurations could be in 3D space and not necessarily in the 2D plane.

The rotations of the beam with BC2 are oriented only around $\overrightarrow{0\beta}$-axis at the first edge while it can freely rotate at the end. As shown in Fig. 4b, the variation of the buckling force is independent of β angle except at $\beta = 0$. As explained before, 3D hinge joint in BC2 behaves as a clamped joint for $\beta = 0$. It should be noted that, by slightly change in β angle from zero, the buckling force drops extremely from $2.04f_c$ to f_c. In reality, it can be considered that β angle never gets exactly zero value while there is always some clearance in joints. Therefore, the buckling mode corresponds with simply-supported boundary conditions of the Euler beam.

Beams under BC3 are constrained by 3D hinge joints at both ends. The rotations are limited around $\overrightarrow{\alpha\beta}$-axis at the first edge while it can rotate along x_3-axis at the end. The variation of critical in-plane force for beams with BC3 is shown for circular and rectangular cross sections in Fig. 4c and 4d, respectively. For this condition and specially for beams with the circular cross section, the effect of β angle on the buckling load is dominant compared with α angle. As can be seen in Fig. 4c, $\overrightarrow{\alpha\beta}$-axis with $\beta = \frac{\pi}{2}$ orients along the x_3-axis, therefore the buckling force and corresponding shape mode are the same with the 1st mode of Euler simply-supported beams. It should also be noted that the buckling force and the shape mode for BC3 in case of $\beta = 0$ are independent of α angle which is similar to the 1st mode of clamp-simply-supported beams. As shown in Fig. 4d, the

distribution of the buckling force for beams with rectangular cross section and BC3 are affected by the area moment of inertia of the cross section. In other words, by changing the direction of rotation at the 3D hinge, the effective area moment of inertia changes as well.

The buckling forces, as shown in Fig. 4, have been obtained for various boundary conditions using the linear model. This estimation of buckling force and mode shape will be used as an initial configuration for determining post-buckling paths. Fig. 5 shows the post-buckling paths and corresponding 3D configurations with distribution of von-Mises stress for beams with BC1. For all cases, the beam configuration starts from the $x_1 - x_2$ plane, but by increasing the in-plane load, the configuration transforms into the 3D space. As mentioned before, 3D hinge joint with $\beta = 0$ reacts like clamped support in the small deformation regime. Fig. 5a and 5b demonstrates that the bifurcation point for the 3D hinge support occurs earlier than that for fully clamped boundary conditions. Since the beam can freely rotate along its axis at the first end, there is no torsional stiffness against transformation from 2D to 3D configuration. On the other hand, there is not any bifurcation points for other boundary conditions while by increasing the in-plane load, the beam tends to rotate along its axis and transform into 3D configuration, see Fig. 5c-5f. In 3D hinge with $0 < \beta < \frac{\pi}{2}$, the in-plane load generates the rotational moment at the hinge which turns the beam from the $x_1 - x_2$ plane into the 3D space. The effects of the 3D hinge can be more emphasized by comparing post-buckling path of beams with BC1 with $\beta/\pi = 0.375$ and 0.5. In this case, the path of out-of-plane displacement and beam configuration are obviously different even though they show close buckling force and in-plane displacement path.

The response of beams with BC2 subjected to in-plane load is displayed in Fig. 6. In spite of similar critical force and buckling mode shape (see Fig. 4b), the post-buckling paths and beam configurations are entirely different. It is obvious that the beam with BC2 with $\beta/\pi = 0$ and 0.5 follows paths of clamped-simply-supported and fully simply-supported in plane space, respectively. For the other cases, there are 3D post-buckling configurations. It can be seen after the first buckling at f_c, the beam experiences a bifurcation point in the post-buckling path. In fact, this bifurcation point happens after the first buckling point following bending/twisting path naturally and without any enforcement or guidance. The beam initially deforms in the $x_1 - x_2$ plane and then by increasing the in-plane load, it starts turning around its axis for $\frac{\pi}{2}$ radian approximately, see Fig. 6b. That is because of high coupling between bending and torsion combined with the effects of 3D hinge joint to generate a twisting moment. It should also be highlighted that post-buckling loads show different values after passing the buckling point, and the shape mode configuration changes during this path that is unlike what the linear model predicts.

The post-buckling paths of beams with BC3 are investigated in three sections. BC4, BC5 and BC6 can be considered as special cases of BC3. The post-buckling paths and beam configurations for BC4 subjected to in-plane loads are shown in Fig. 7. The variation of buckling force can be tracked on Fig. 4c where $\alpha = 0$ and β increases from 0 to $\frac{\pi}{2}$. For this boundary condition, the beam rotations are constrained around $\overrightarrow{0\beta}$-axis at the first edge, and x_3-axis at the

end. Therefore, the beam configuration starts changing from the x_1-x_2 plane, and then depending on the value of β angle, it can either remain in the same plane or transfer into 3D space. With a similar scenario, the beam tends to rotate around its axis after the buckling point in spite of resistance of hinge supports at both ends. It should be mentioned that the value of buckling point as well as post-buckling path highly depend on the hinge β angle.

Next, a post-buckling analysis of beams with BC5 is presented in Fig. 8. The buckling forces have been predicted as shown in Fig. 4c where $\beta = 0$ and α increases from 0 to $\frac{\pi}{2}$. Except beams with BC5 and $\alpha = 0$, other beams start changing shape from the $x_1 - x_3$ plane predicted by the linear model. It should be noted that despite same buckling force predicted by the linear model, the post-buckling paths are different. It is seen in Fig. 8 that, when beams buckle, their configurations transfer from 2D plane to 3D space. Except the beam with BC5 and $\alpha = 0$, the other beams experience snap-bucking phenomenon around the buckling point. In other words, after passing the buckling point, the buckling load decreases gradually. In this case, the coupling between bending and torsion as well as 3D hinge joints have significant effects on the post-buckling paths and beam configurations.

Finally, tracking post-buckling paths of beams with BC6 is investigated in Fig. 9. The result of the linear model for this case can be found in Fig. 4c where $\alpha = \frac{\pi}{2}$ and β increases from 0 to $\frac{\pi}{2}$. In this case, the beam configurations have been predicted in the 3D space by the linear model. It is observed that, the buckling forces as well as out-of-plane deformations directly depend on the hinge β angle, see Fig. 9a and 9b. Except beams with BC6 and $\beta = 0$, the other cases under proportional out-of-plane deformation experience post-buckling paths in the same direction of buckling mode shapes, see Fig. 9b.

4.3. Straight beam under torsion

In this section, the behavior of beams with BC7 and BC8 subjected to torsional loadings is investigated. BC7 has 3D hinge-hinge supports and it is constrained at $x_1 = L$ to move and rotate along the beam axis and can only rotate around $\overrightarrow{0\beta}$-axis at $x_1 = 0$.

As shown in Fig. 10, in the first step, the beam is twisted with an out-of-plane rotation via applying a torque at $x_1 = L$. As explained in the previous section, there is a high coupling between bending and torsion in the 3D beam structures especially with 3D hinge supports. This loading step will continue to return a point at D where the beam turns around its axis. After passing the first return point, the torsional torque decreases to get a negative value till it meets the 2nd return point at F. In this stage, the beam turns around its axis to get back to the initial configuration. It should be noted that all these stages somehow can be detected for all β angles in beams with BC7. As can be seen, Riks technique successfully captures torque-angle paths whereas the usual Newton-Raphson method fails to follow paths after the 1st return point.

5. Conclusion

The exact displacement field were proposed based on the central point movement and orthogonal rotation functions. The Cauchy-Green deformation adapted for the 2nd Piola–Kirchhoff stress tensors was extracted through the continuum mechanics framework. The finite element formulation was developed based on the exact 3D beam deformation field. The elemental vectors and matrices were modified according to centroid forces and moments in the 3D Cartesian coordinate system. The present finite element format is adapted with other 2D or linear beam theories as well as 3D boundary conditions. After assembling the elemental vectors and matrices, the system of equilibrium equations were obtained in the global coordinate. The solution process was done by taking advantage of Newton-Raphson method and Riks technique. The post-buckling response of the fully clamped beam was studied for verification of the present model and finite element formulation. The comparison study revealed a good overview of robustness and accuracy of the presented model. The effects of 3D hinge supports on the large-deformation instability of beams under axial and torsional loadings were studied. It was observed that the post-buckling paths as well as beam configuration are highly affected by torsion and bending coupling. This coupling can be strengthened when the beam is constrained by 3D hinge supports. It was found that the linear model can not provide accurate estimations of the beam behavior under complicated boundary conditions. It was seen that, in some cases, the post-buckling paths and configuration modes are transformed upon passing the buckling point. It was also highlighted that in-plane loads turn the beam around its axis due to generating torque at 3D hinges. It was observed that in-plane load decreases after passing the buckling point which can make a snap point in a load-control path. The high coupling between torsion and bending was also observed in beams with 3D hinge supports under torsional moments. It was concluded that the torsional deformation can raise the bending stiffness up extremely. In these cases, robustness and accuracy of the present model were examined showing good and efficient outcomes. Due to lack of similar work in the literature, the formulation, solution and results of this research are expected to contribute to understanding of the stability behaviors and to be instrumental in design of 3D beams supported with 3D hinge joints under axial and torsional loadings.

References

[1] E. Reissner, On one-dimensional large-displacement finite-strain beam theory, Studies Appl. Math. 52 (1973) 87-95.

[2] E. Reissner, On finite deformation of space curved beams, J. Appl. Math. Phys. 32 (1981) 734–744.

[3] J. C. Simo, A finite strain beam formulation. The three-dimensional dynamic problem, Part I, Comput. Methods Appl. Mech. Engrg. 49 (1985) 55–70.

[4] K.J. Bathe, S. Bolourchi, Large displacement analysis of three dimensional beam structures, Int. J. Num. Methods Eng. 14 (1979) 961-986.

[5] H. Irschik, G. Johannes, A continuum mechanics based derivation of Reissner's large-displacement finite-strain beam theory: the case of plane deformations of originally straight Bernoulli–Euler beams, Acta Mech. 206, no. 1-2 (2009): 1–21.

[6] E. Zupan, M. Saje, D. Zupan, On a virtual work consistent three-dimensional Reissner–Simo beam formulation using the quaternion algebra, Acta Mech. 224, no. 8 (2013) 1709–1729.

[7] G. Kirchhoff, Ueber das Gleichgewicht und die Bewegung eines unendlich dunnen elastischen Stabes, J. Reine Angew. Math. 56 (1859) 285–313.

[8] A. Ibrahimbegovic, On the finite element implementation of geometrically non-linear Reissner's beam theory: 3d curved beam element, Comput. Methods Appl. Mech. Engrg. 122 (1995) 11–26.

[9] C. Meier, A. Popp, W. A. Wall, An objective 3D large deformation finite element formulation for geometrically exact curved Kirchhoff rods, Comput. Methods Appl. Mech. Engrg. 278 (2014) 445–478.

[10] C. Meier, A. Popp, W. A. Wall, A locking-free finite element formulation and reduced models for geometrically exact Kirchhoff rods, Comput. Methods Appl. Mech. Engrg. 290 (2015) 314–341.

[11] D.H. Hodges, Lateral-torsional flutter of a deep cantilever loaded by a lateral follower force at the tip, Journal of Sound and Vibration, 247(1) (2001) 175-183.

[12] W. Yu, D.H. Hodges, V.V. Volovoi, E.D. Fuchs, A generalized Vlasov theory for composite beams, Thin-Walled Structures, 43(9) (2005) 1493-1511.

[13] C. Pacoste, A. Eriksson, Beam elements in instability problems, Comput. Methods Appl. Mech. Eng. 144 (1997) 163–197.

[14] M.A. Crisfield, A consistent co-rotational formulation for non-linear, three-dimensional, beam-elements, Comput. Methods Appl. Mech. Eng. 81 (1990) 131–150.

[15] K. M. Hsiao, W. Y. Lin, A co-rotational finite element formulation for buckling and postbuckling analyses of spatial beams, Comput. Methods Appl. Mech. Engrg. 188 (2000) 567-594.

[16] Z.X. Li, L. Vu-Quoc, A mixed co-rotational 3d beam element formulation for arbitrarily large rotations, Adv. Steel Constr. 2 (2010) 767-787.

[17] F.N. Gimena, P. Gonzaga, L. Gimena, Stiffness and transfer matrices of a non-naturally curved 3D-beam element, Eng. Struct. 30 (2008) 1770–1781.

[18] A. R. Damanpack, M. Bodaghi, W. H. Liao, A robust hyper-elastic beam model under bi-axial normal-shear loadings, Int. J. of NonLin. Mech. 95 (2017) 287-295

[19] S. N. Atluri, M. Iura, S. Vasudevan, A consistent theory of finite stretches and finite rotations in space-curved beams of arbitrary cross-section, Comput. Mech. 27 (2001) 271-281.

[20] H.B. Coda, A solid-like FEM for geometrically non-linear 3D frames, Comput. Methods Appl. Mech. Eng. 198 (2009) 3712–3722.

[21] D. Manta, R. Goncalves, A geometrically exact Kirchhoff beam model including torsion warping, Comput. Struct. 177 (2016) 192–203.

[22] D. Vo, P. Nanakorn, A total Lagrangian Timoshenko beam formulation for geometrically nonlinear isogeometric analysis of planar curved beams, Acta Mech. (2020) 1–21.

[23] N. Liu, W. Yu, D. H. Hodges, Mechanics of structure genome-based global buckling analysis of stiffened composite panels, Acta Mech. 230, no. 11 (2019): 4109-4124.

[24] A. Cardona, A. Huespe, Evaluation of simple bifurcation points and post-critical path in large finite rotation problems, Comput. Methods Appl. Mech. Engrg. 175 (1999) 137-156.

[25] S. V. Levyakov, Formulation of a geometrically nonlinear 3D beam finite element based on kinematic- group approach, Appl. Math. Model. 39 (2015) 6207-6222.

[26] M. Liao, F. Chen, Z. Chen, Y.B. Yang, A weak-form quadrature element formulation for 3D beam elements used in nonlinear and postbuckling analysis of space frames, Eng. Struct. 145 (2017) 34–43.

[27] E. Cottanceau, O. Thomasa, P. Veron, M. Alochet, R. Deligny, A finite element/quaternion/asymptotic numerical method for the 3D simulation of flexible cables, Finite Elem. Anal. and Des. 139 (2018) 14–34.

[28] R. Gonçalves, An assessment of the lateral-torsional buckling and post-buckling behaviour of steel I-section beams using a geometrically exact beam finite element, Thin. Wall. Struct. 143 (2019) 106-222.

[29] O. Weeger, B. Narayanan, M. L. Dunn, Isogeometric shape optimization of nonlinear, curved 3D beams and beam structures, Comput. Methods Appl. Mech. Engrg. 345 (2019) 26-51.

[30] O.C. Zienkiewicz, R. L. Taylor. The finite element method, McGraw Hill, London, 1994.

[31] J.N. Reddy, An Introduction To nonlinear finite element analysis, Oxford University Press, New York, 2004.

List of Figures:

Table 1. Description of 3D nodal boundary conditions

3D hinge type	Displacement boundary		Rotation boundary	
	Symbol	Conditions	Symbol	Conditions
Movements/rotations along 3 axes	$_-H$	$f_1 = f_2 = f_3 = 0$	H_-	$m_1 = m_2 = m_3 = 0$
Movements/rotations along 2 axes	$_{\overline{\alpha_1\beta_1}}^{\overline{\alpha_2\beta_2}}H$	$\left(\overrightarrow{\alpha\beta} = \overrightarrow{\alpha_1\beta_1} \times \overrightarrow{\alpha_2\beta_2}\right)$ $u_{1\overrightarrow{\alpha\beta}} = 0$	$H_{\overline{\alpha_1\beta_1}}^{\overline{\alpha_2\beta_2}}$	$\left(\boldsymbol{q}_{\overrightarrow{\alpha\beta}} = \boldsymbol{q}_{\overrightarrow{\alpha_1\beta_1}}\boldsymbol{q}_{\overrightarrow{\alpha_2\beta_2}}\right)$ $q_{33\overrightarrow{\alpha\beta}} = q_{11\overrightarrow{\alpha\beta}}q_{22\overrightarrow{\alpha\beta}}$
Movement/rotation along 1 axis	$_{\overrightarrow{\alpha_1\beta_1}}H$	$u_{2\overrightarrow{\alpha_1\beta_1}} = u_{3\overrightarrow{\alpha_1\beta_1}} = 0$	$H_{\overrightarrow{\alpha_1\beta_1}}$	$\left(\boldsymbol{q} = \boldsymbol{q}_{\overrightarrow{\alpha_1\beta_1}}\right)$ $q_{11\overrightarrow{\alpha_1\beta_1}} = 1;\ q_{12\overrightarrow{\alpha_1\beta_1}} = 0$
Fixed in 3 axes	$_cH$	$u_1 = u_2 = u_3 = 0$	H_C	$(\boldsymbol{q} = \boldsymbol{I})$ $q_{11} = q_{22} = q_{33} = 1$
$(\alpha = 0, \beta = 0) \rightarrow x_1$	$\left(\alpha = \frac{\pi}{2}, \beta = 0\right) \rightarrow x_2$		$\left(\alpha = \alpha_0, \beta = \frac{\pi}{2}\right) \rightarrow x_3$	

Table 2. Boundary conditions

Case / Location	BC1	BC2	BC3	BC4	BC5	BC6	BC7	BC8
$x_1 = 0$	$_cH_{\overrightarrow{0\beta}}$	$_cH_{\overrightarrow{0\beta}}$	$_cH_{\overrightarrow{\alpha\beta}}$	$_cH_{\overrightarrow{0\beta}}$	$_cH_{\overrightarrow{\alpha 0}}$	$_cH_{\overrightarrow{\pi\beta}}$	$_cH_{\overrightarrow{0\beta}}$	$_cH_{\overrightarrow{0\beta}}$
$x_1 = L$	$_{x_1}H_C$	$_{x_1}H_-$	$_{x_1}H_{x_3}$	$_{x_1}H_{x_3}$	$_{x_1}H_{x_3}$	$_{x_1}H_{x_3}$	$_{x_1}H_{x_1}$	$_cH_{x_1}$

List of Figures:

Fig. 1. Coordinate system and kinematics of the geometrically exact beam model: (a) displacements, (b) rotations.

Fig. 2. (a) 3D beam element and (b) 3D support model.

Fig. 3. Comparison between 2D and 3D behaviors of a fully clamped beam under an in-plane axial load: maximum out-of-plane displacements path.

Fig. 4. The buckling force of beams with different boundary conditions: the circular cross section under (a) BC1, (b) BC2, (c) BC3; the rectangular cross section under BC3 (d).

Fig. 5. The post-buckling path and configuration at $\frac{u_1}{L} = 20\%$, 40% and 60% for beams with BC1: (a) in-plane force path with displacement; (b) maximum out-of-plane displacements path; beam configuration with von-Misses stress distribution (MPa) for (c) $\beta/\pi = 0$, (d) $\beta/\pi = 0.125$, (e): $\beta/\pi = 0.375$, and (f) $\beta/\pi = 0.5$.

Fig. 6. The post-buckling path and configuration at $\frac{u_1}{L} = 10\%$, 30% and 60% for beams under BC2: (a) in-plane force path with displacement; (b) maximum out-of-plane displacements path; the beam configuration with von-Misses stress distribution (MPa) for (c) $\beta/\pi = 0$, (d) $\beta/\pi = 0.1$, (e) $\beta/\pi = 0.25$ and (f) $\beta/\pi = 0.5$.

Fig. 7. The post-buckling path and configuration at $\frac{u_1}{L} = 20\%$, 40% and 60% for beams with BC4: (a) in-plane force path with displacement; (b) maximum out-of-plane displacements path; the beam configuration with von-Misses stress distribution (MPa) for (c) $\beta/\pi = 0$, (d) $\beta/\pi = 0.125$, (e) $\beta/\pi = 0.375$ and (f) $\beta/\pi = 0.5$.

Fig. 8. The post-buckling path and configuration at $\frac{u_1}{L} = 20\%$, 40% and 60% for beams with BC5: (a) in-plane force path with displacement; (b) maximum out-of-plane displacements path; the beam configuration with von-Misses stress distribution (MPa) for (c) $\alpha/\pi = 0$, (d) $\alpha/\pi = 0.125$, (e) $\alpha/\pi = 0.375$ and (f) $\alpha/\pi = 0.5$.

Fig. 9. The post-buckling path and configuration at $\frac{u_1}{L} = 20\%$, 40% and 60% for beams with BC6: (a) in-plane force path with displacement; (b) maximum out-of-plane displacements path; the beam configuration with von-Misses stress distribution (MPa) for (c) $\beta/\pi = 0$, (d) $\beta/\pi = 0.125$, (e) $\beta/\pi = 0.375$ and (f) $\beta/\pi = 0.5$.

Fig. 10. The torque path with twisting angle and configuration for beams with BC7: (a) torsional moment path with twisting angle; (b) bending moment path with twisting angle; (c) the beam configuration with von-Misses stress distribution (MPa) for $\beta/\pi = 0.3$.
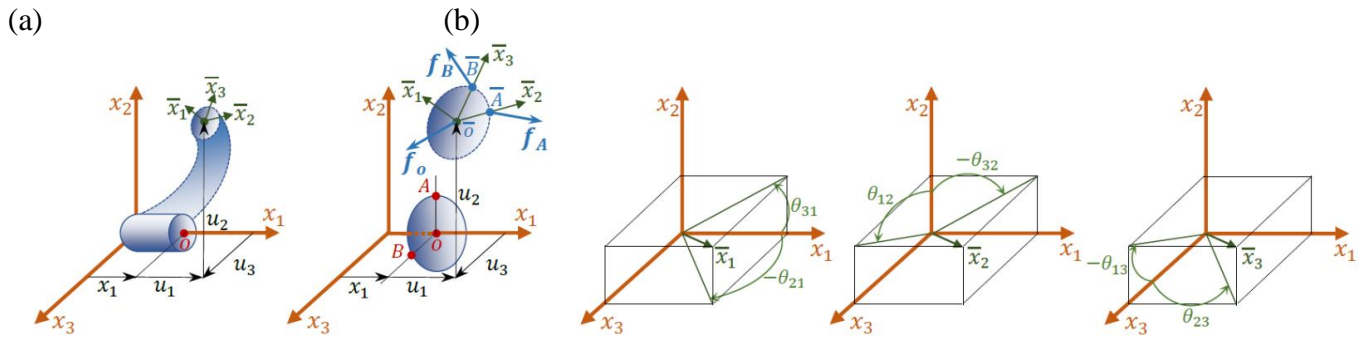
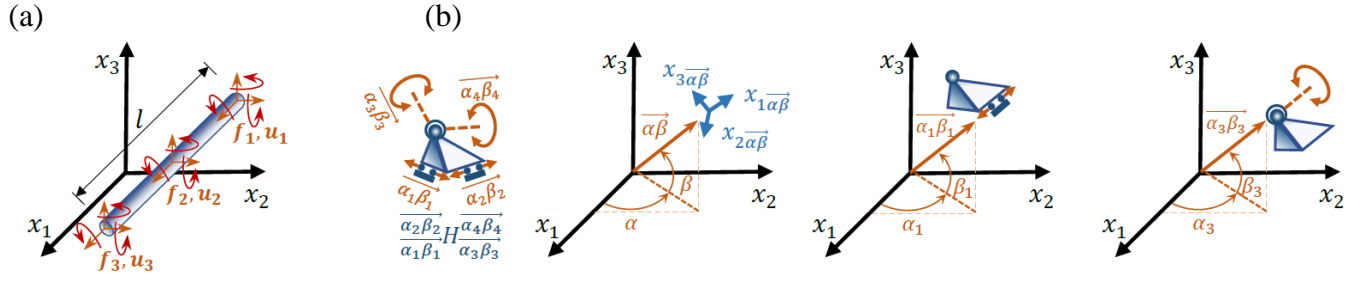**Fig. 1.** Coordinate system and kinematics of the geometrically exact beam model: (a) displacements, (b) rotations.
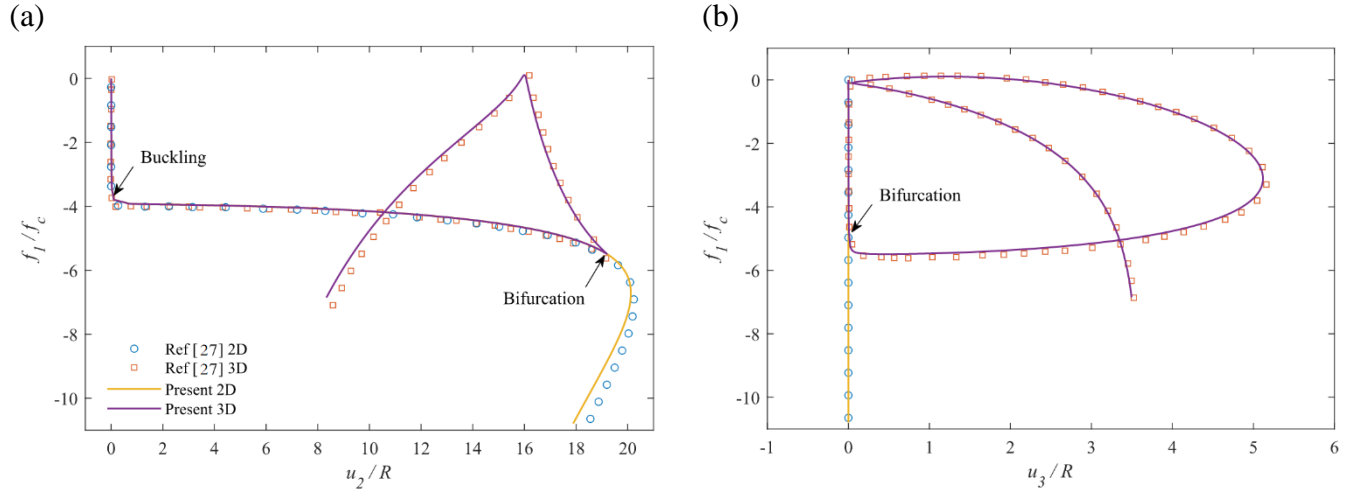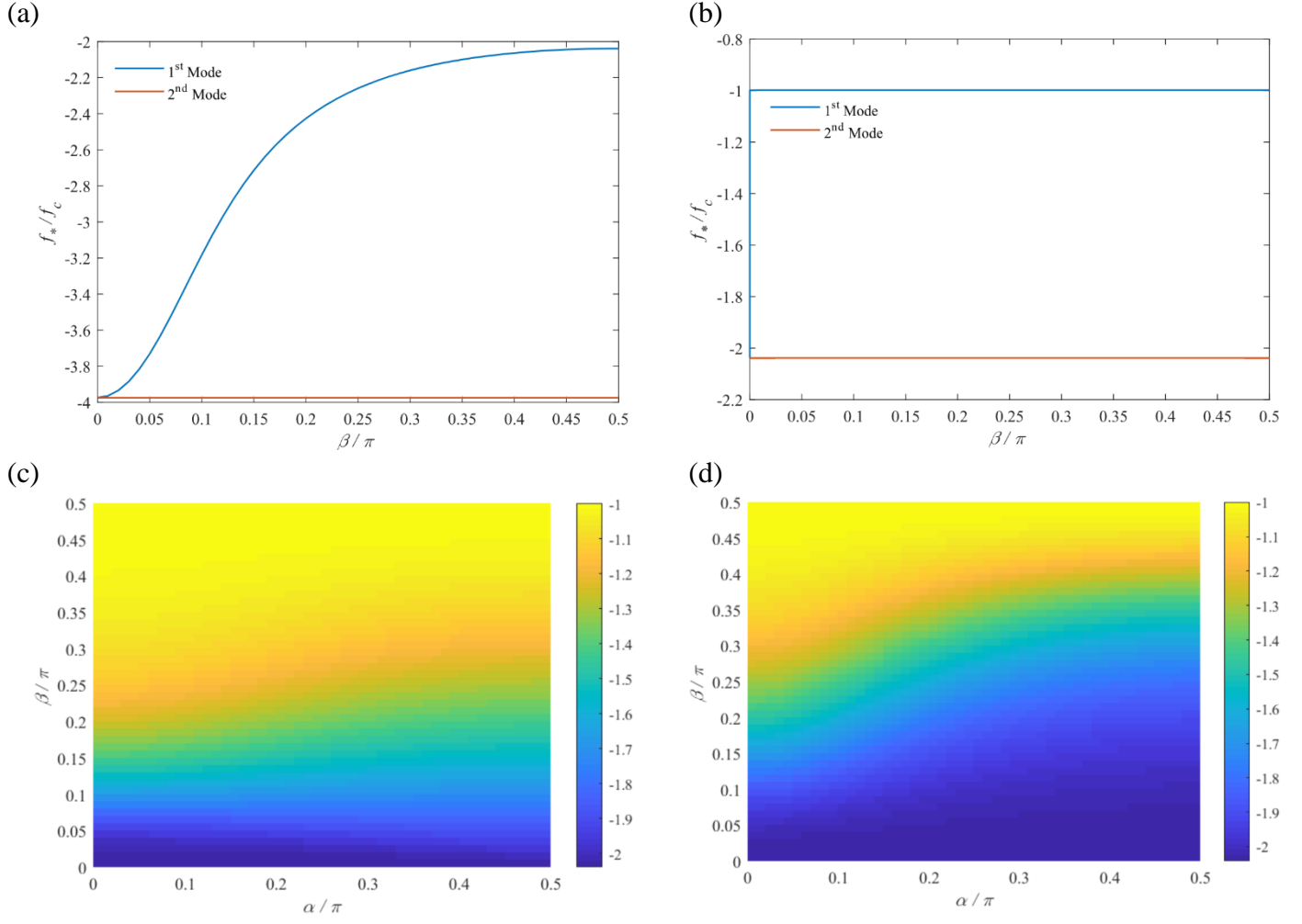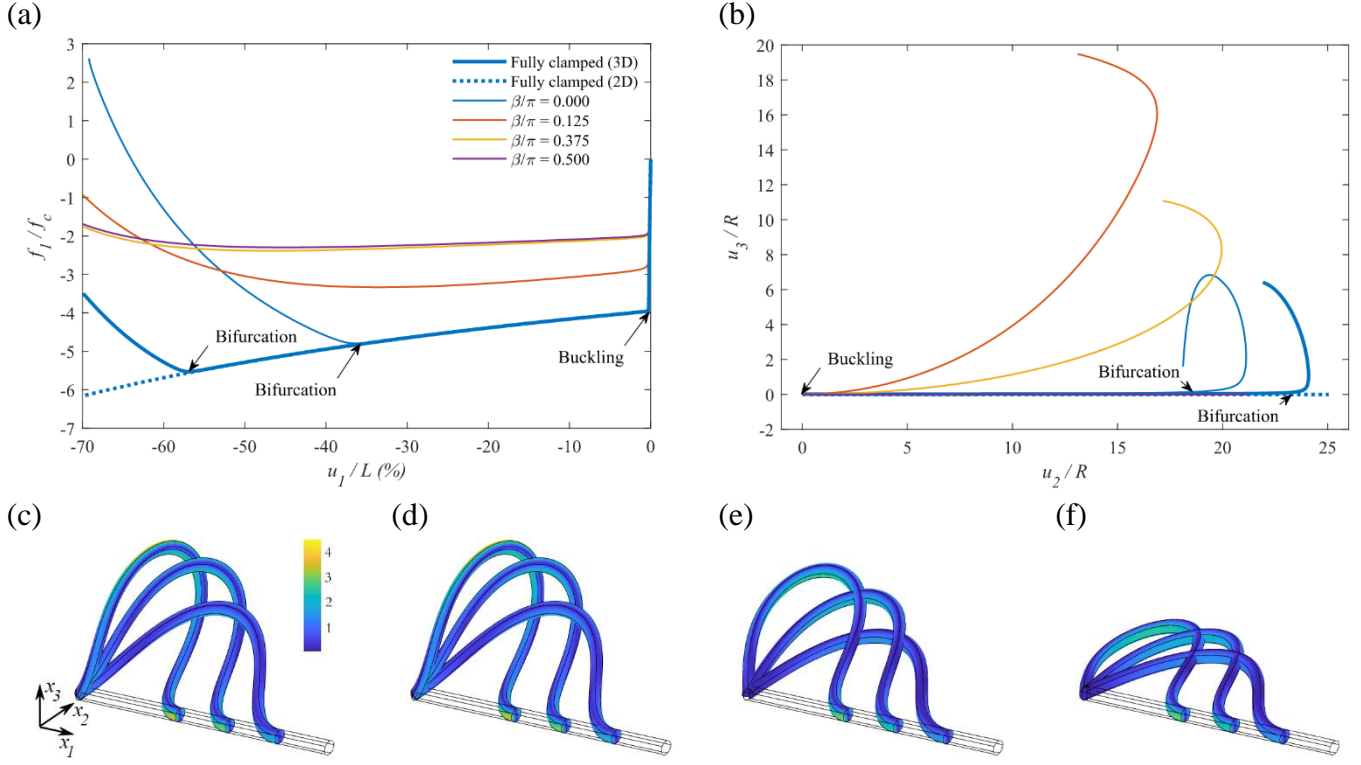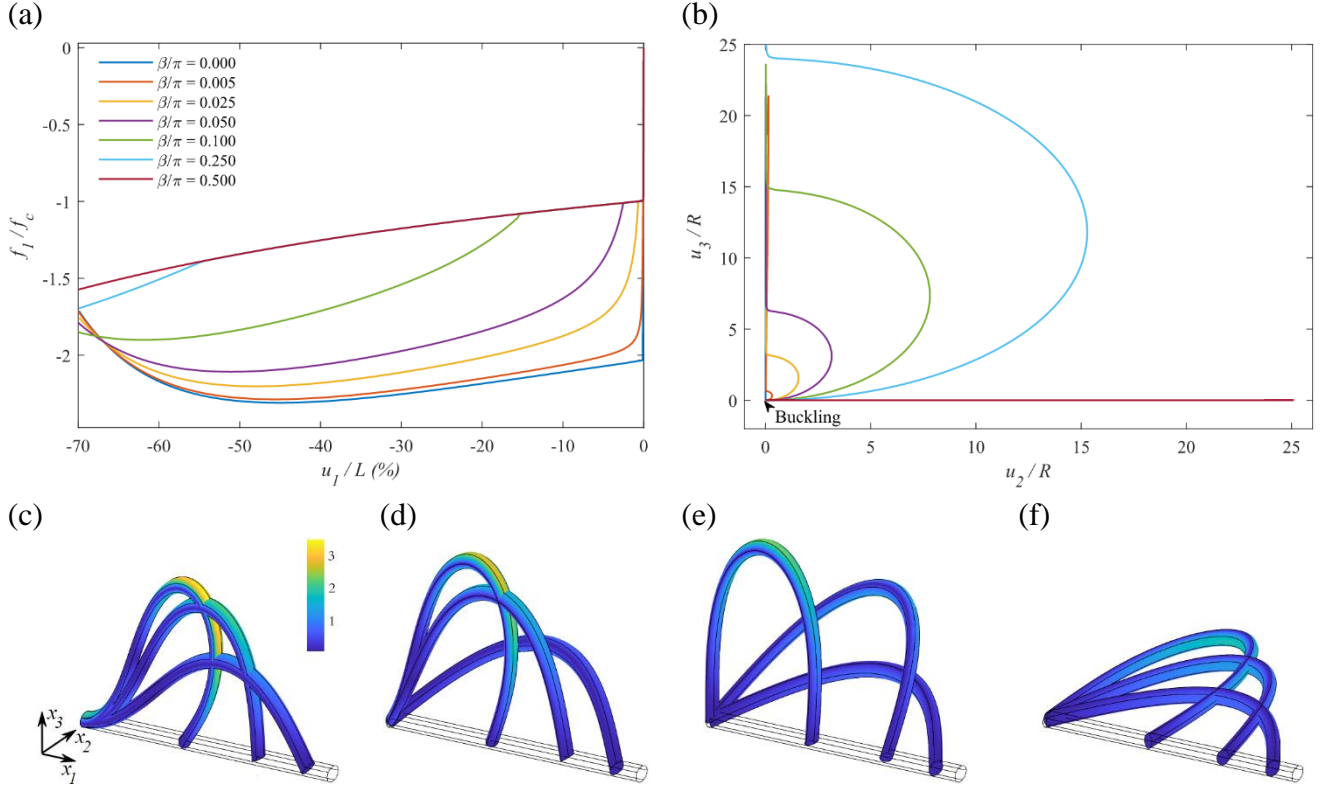
Fig. 2. (a) 3D beam element and (b) 3D support model.

Fig. 3. Comparison between 2D and 3D behaviors of a fully clamped beam under an in-plane axial load: maximum out-of-plane displacements path.

Fig. 4. The buckling force of beams with different boundary conditions: the circular cross section under (a) BC1, (b) BC2, (c) BC3; the rectangular cross section under BC3 (d).
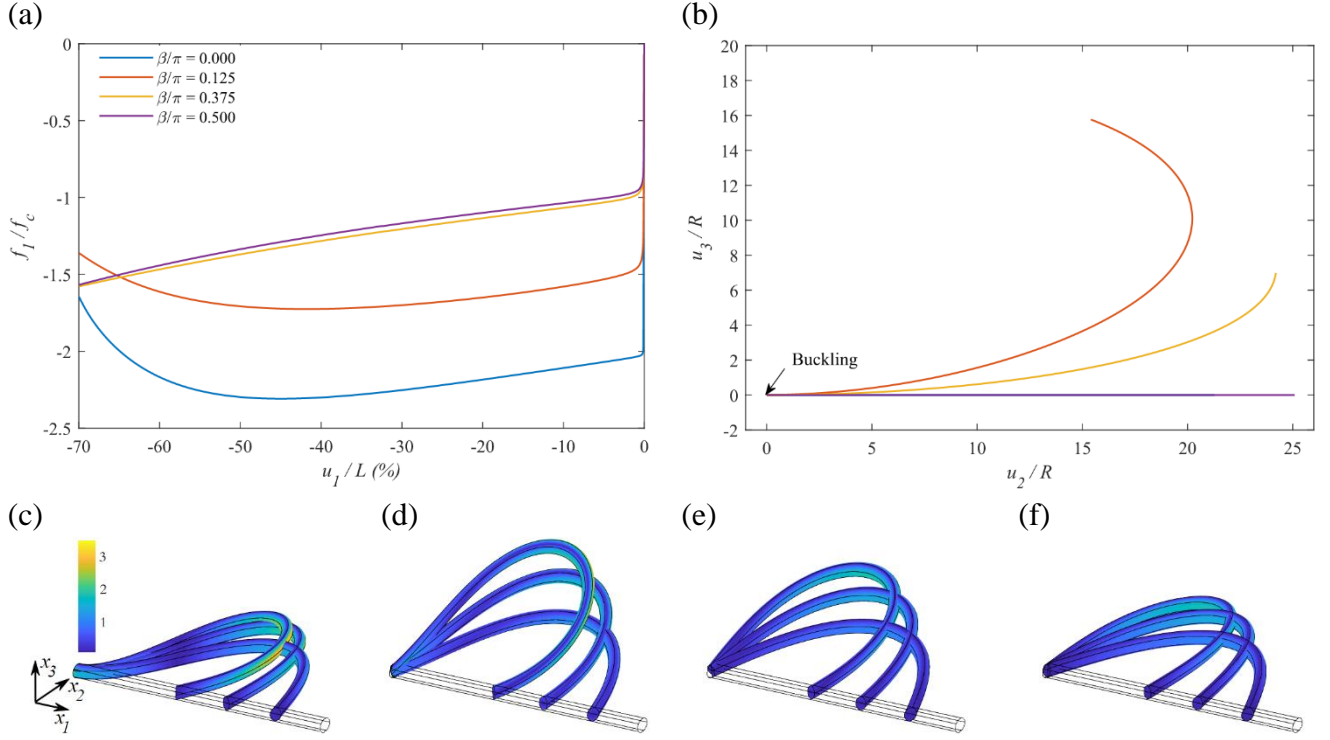
Fig. 5. The post-buckling path and configuration at $\frac{u_1}{L} = 20\%$, 40% and 60% for beams with BC1: (a) in-plane force path with displacement; (b) maximum out-of-plane displacements path; beam configuration with von-Misses stress distribution (MPa) for (c) $\beta/\pi = 0$, (d) $\beta/\pi = 0.125$, (e): $\beta/\pi = 0.375$, and (f) $\beta/\pi = 0.5$.

Fig. 6. The post-buckling path and configuration at $\frac{u_1}{L} = 10\%$, 30% and 60% for beams under BC2: (a) in-plane force path with displacement; (b) maximum out-of-plane displacements path; the beam configuration with von-Misses stress distribution (MPa) for (c) $\beta/\pi = 0$, (d) $\beta/\pi = 0.1$, (e) $\beta/\pi = 0.25$ and (f) $\beta/\pi = 0.5$.
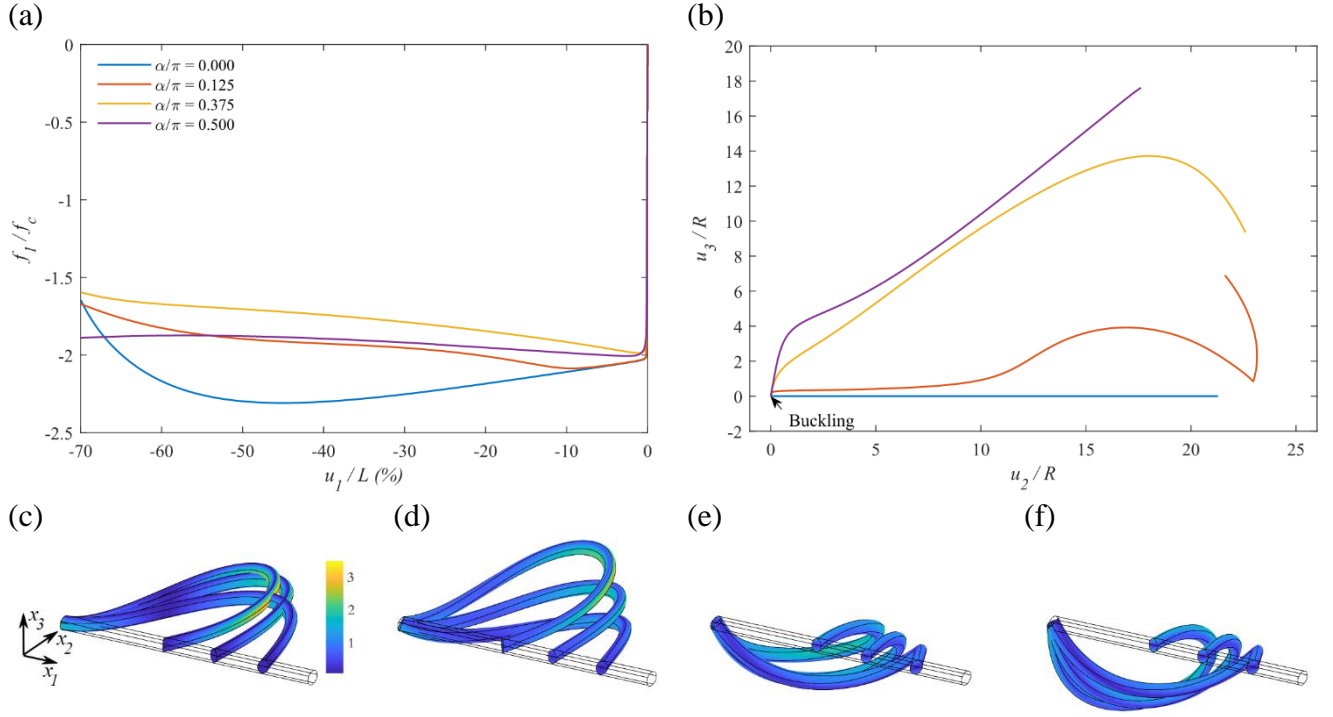
Fig. 7. The post-buckling path and configuration at $\frac{u_1}{L} = 20\%$, 40% and 60% for beams with BC4: (a) in-plane force path with displacement; (b) maximum out-of-plane displacements path; the beam configuration with von-Misses stress distribution (MPa) for (c) $\beta/\pi = 0$, (d) $\beta/\pi = 0.125$, (e) $\beta/\pi = 0.375$ and (f) $\beta/\pi = 0.5$.

Fig. 8. The post-buckling path and configuration at $\frac{u_1}{L} = 20\%$, 40% and 60% for beams with BC5: (a) in-plane force path with displacement; (b) maximum out-of-plane displacements path; the beam configuration with von-Misses stress distribution (MPa) for (c) $\alpha/\pi = 0$, (d) $\alpha/\pi = 0.125$, (e) $\alpha/\pi = 0.375$ and (f) $\alpha/\pi = 0.5$.
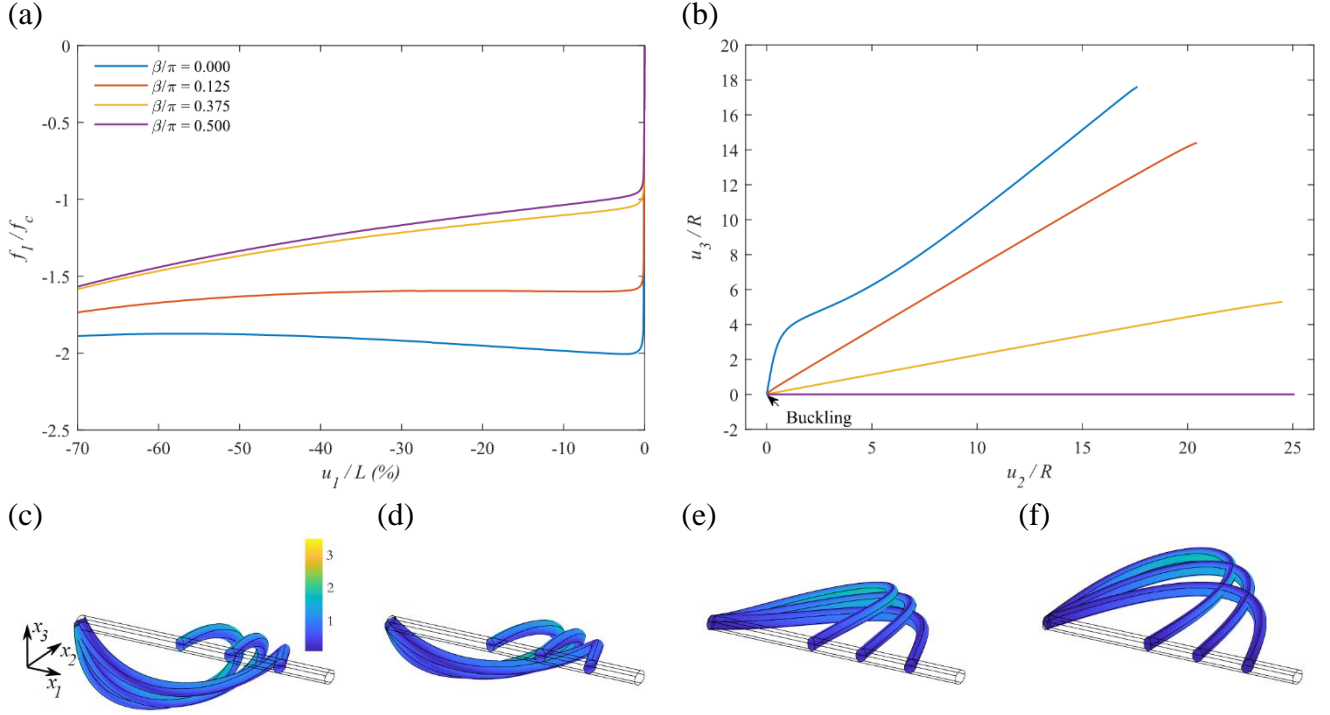
Fig. 9. The post-buckling path and configuration at $\frac{u_1}{L} = 20\%$, 40% and 60% for beams with BC6: (a) in-plane force path with displacement; (b) maximum out-of-plane displacements path; the beam configuration with von-Misses stress distribution (MPa) for (c) $\beta/\pi = 0$, (d) $\beta/\pi = 0.125$, (e) $\beta/\pi = 0.375$ and (f) $\beta/\pi = 0.5$.
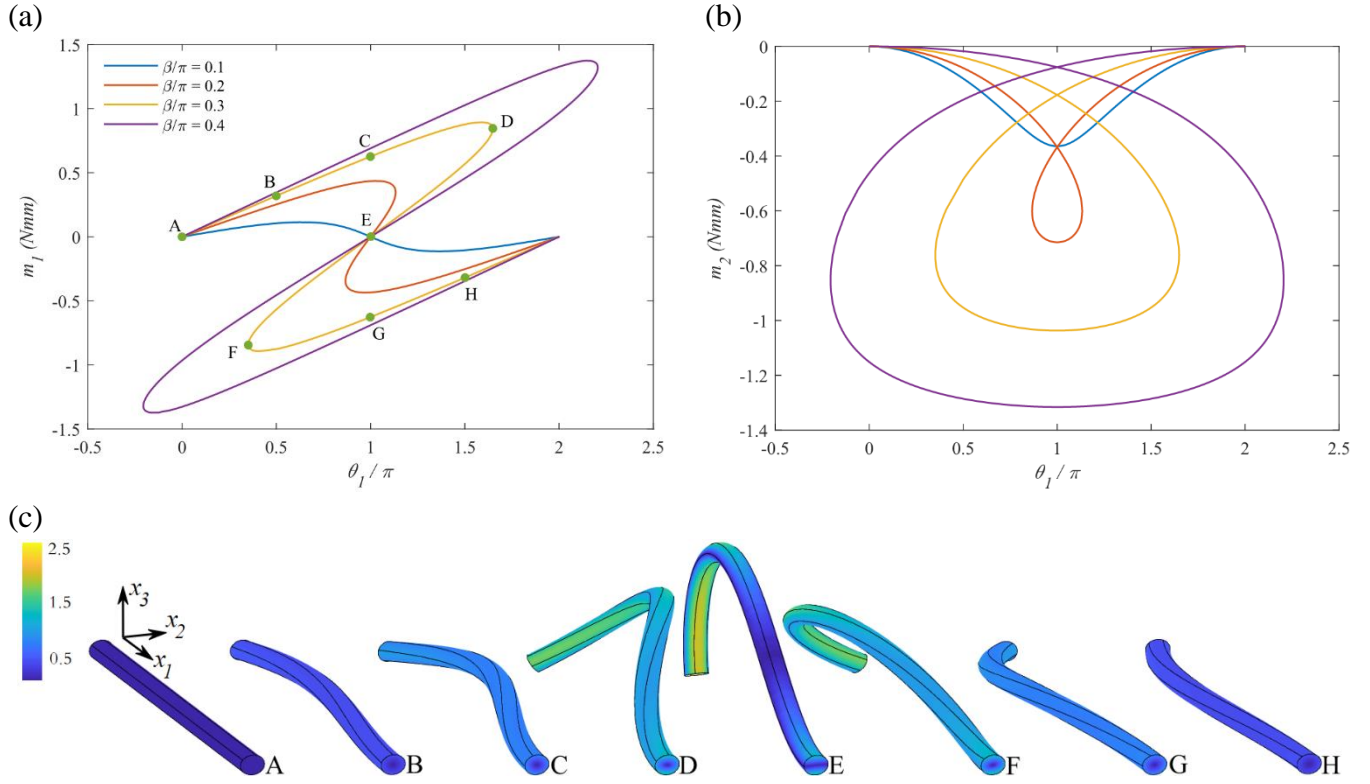
Fig. 10. The torque path with twisting angle and configuration for beams with BC7: (a) torsional moment path with twisting angle; (b) bending moment path with twisting angle; (c) the beam configuration with von-Misses stress distribution (MPa) for $\beta/\pi = 0.3$.